

# Holographic deep thermalization

Bingzhi Zhang,<sup>1,2,\*</sup> Peng Xu,<sup>3</sup> Xiaohui Chen,<sup>4</sup> and Quntao Zhuang<sup>2,1,†</sup>

<sup>1</sup>*Department of Physics and Astronomy, University of Southern California, Los Angeles, California 90089, USA*

<sup>2</sup>*Ming Hsieh Department of Electrical and Computer Engineering,*

*University of Southern California, Los Angeles, California 90089, USA*

<sup>3</sup>*Department of Statistics, University of Illinois at Urbana-Champaign, Champaign, IL 61820, USA*

<sup>4</sup>*Department of Mathematics, University of Southern California, Los Angeles, California 90089, USA*

Random quantum states play a critical role in quantum information processing. While random quantum circuits typically provide pseudo-random states, deep thermalization introduces quantum measurement to generate genuinely random states. However, the requirement of large ancillae in conventional deep thermalization poses a challenge to scale up the system size. We introduce holographic deep thermalization to substantially reduce the required ancillae to a system-size independent constant. Our circuit design trades space with time, via adopting a sequential application of an scrambling-measure-reset process on a small number of ancillae. Via tuning the ancilla size and number of time steps, holographic deep thermalization allows a continuous trade-off between the total quantum circuit size and the ancilla size. In the case of finite-size systems, we further enhance the performance of holographic deep thermalization via generative quantum machine learning, which leads to constant-factor advantages in the convergence towards Haar random. The theoretical predictions are verified with IBM Quantum noisy simulations.

Randomness is an essential resource in information processing and physics. Classical randomness forms the underlying foundation of cryptography, generative machine learning and thermodynamics, while quantum randomness is crucial for quantum information scrambling [1], variational quantum algorithms [2, 3], quantum dynamics [4–6], quantum cryptography [7] and quantum learning [8, 9]. The unique type of random quantum states necessary in these scenarios is the Haar random ensemble uniformly distributed over the entire Hilbert space. They are particularly important as they represent the typical quantum states in the Hilbert space, with high complexity and volume-law entanglement. For the same reason, though, they are also difficult to generate.

Several approaches have been developed to generate Haar random states, or more specifically, their approximate version up to the  $K$ -th moment—approximate  $K$ -design states. It is proved in Refs. [10, 11] that one can generate  $K$ -design states of  $N_A$  qubits via local random unitary circuits with depth  $\sim \text{poly}(K)N_A$ . However, generating different samples is achieved by randomly adjusting the quantum gates, leading to significant overhead in quantum circuit compilation and experimentation. More importantly, such approaches only generate pseudo-random quantum states, whenever the classical random numbers involved are typically pseudo-random.

Recently, the emergent state design in ‘deep thermalization’ (DT) [5] suggests a promising approach to generate genuinely random states from partial quantum measurement, with the initial state and quantum dynamics both fixed. The  $K$ -design state ensemble emerges within a small subsystem via projective measurement over the rest majority of qubits when the whole system sufficiently

thermalizes via a chaotic Hamiltonian dynamics. Though the chaotic Hamiltonian evolution can be implemented on a quantum simulator [12], it generally requires a significant amount of quantum computing resources. In particular, such approaches require a large number of ancilla qubits, casting an experimental challenge considering near-term quantum devices with limited number of qubits [12].

In this work, we introduce the *holographic deep thermalization* (HDT), a new paradigm for generating random quantum states with only a *constant* number of ancilla qubits, via trading space resource with time [13]. More precisely, to achieve  $\epsilon$  relative error of the  $K$ -th frame potential in generating  $N_A$ -qubit Haar random state, our HDT only requires  $K + \log_2(1/\epsilon)$  constant number of ancilla qubits and a time step of  $KN_A/[K + \log_2(1/\epsilon)]$ . In each time step, a fixed Haar random unitary, similar to that in DT yet on a much smaller system size, is applied and then the ancillae are measured and reset. In contrast, conventional DT requires  $KN_A + \log_2(1/\epsilon)$  number of ancilla qubits [4], substantially increasing with system size.

We rigorously prove the convergence of HDT in terms of the first-order frame potential. For higher-order frame potentials, a lower bound is provided and numerically verified with empirical results. Via balancing the ancilla size and number of time steps, HDT achieves a continuous trade-off between the total quantum circuit size and the ancilla size. Besides the minimum-bath operating point, we also identify a minimum-quantum-circuit-size operating point where ancilla size equals the system size. In the case of finite-size systems, we further enhance the performance of HDT via generative quantum machine learning (QML) approach [14], which leads to constant factor advantages in the convergence towards the Haar random ensemble. We verify our theoretical predictions with IBM Quantum noisy simulation, as we present in

\* bingzhiz@usc.edu

† qzhuang@usc.edu

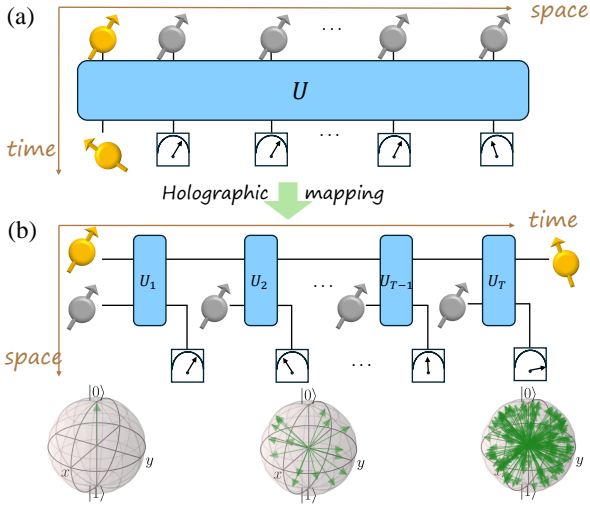


Figure 1. Conceptual plot of (a) deep thermalization with a single chaotic unitary  $U$  and (b) holographic deep thermalization with a sequence of chaotic unitaries  $\{U_t\}_{t=1}^T$ . Yellow and gray represents data and bath systems with qubits  $N_A$  and  $N_B$ .

Appendix.

*Problem set-up and protocol design.*—Generation of genuinely quantum random states in DT relies on the idea of quantum measurement projection. For a fixed pure quantum state  $|\Psi\rangle_{AB}$  on a joint system of  $A$  and  $B$ , the *projected ensemble*  $\mathcal{E}(\Psi)$  on subsystem  $A$  is generated via a projective measurement, with projectors  $\{|z\rangle\langle z|_B\}$  e.g. computational basis, on the rest subsystem  $B$  as [4]

$$\mathcal{E}(\Psi) = \left\{ p_z = \text{tr}(|\Psi\rangle\langle\Psi|_{AB} |z\rangle\langle z|_B), |\psi_z\rangle = \frac{B \langle z|\Psi\rangle_{AB}}{\sqrt{p_z}} \right\}. \quad (1)$$

Indeed, conditioned on the measurement result  $z$  on  $B$ , the state of  $A$  is in a random pure state.

To quantify the closeness of a state ensemble  $\mathcal{E}(\Psi)$  to the Haar random ensemble up to the  $K$ -th moment, we consider its frame potential [6], defined as

$$\mathcal{F}_{\mathcal{E}}^{(K)} \equiv \sum_{z,z'} p_z p_{z'} |\langle \psi_z | \psi_{z'} \rangle|^{2K} \geq \mathcal{F}_{\text{Haar}}^{(K)} = \binom{d_A + K - 1}{d_A - 1}^{-1}, \quad \frac{d_A^2 (d_B + 1)}{d_A^2 d_B + 1} \mathcal{F}_{\text{Haar}}^{(1)} + \frac{(d_A - 1)(d_A d_B - 1)}{d_A^2 d_B + 1} \left( \frac{(d_A^2 - 1) d_B}{d_A^2 d_B^2 - 1} \right)^t. \quad (2)$$

where  $d_A = 2^{N_A}$  is the dimension of the  $N_A$ -qubit system  $A$ . The frame potential quantifies the inversely occupied symmetric space dimension and is thus lower bounded by the Haar ensemble.

When an ensemble achieves the minimum frame potential  $\mathcal{F}_{\text{Haar}}^{(K)}$ , one regards the ensemble as the  $K$ -design [1, 4–6], which approximates the Haar random ensemble to at least the  $K$ -th moment. An  $\epsilon$ -approximate  $K$ -design state ensemble  $\mathcal{E}$  is defined via the relative deviation of frame potential as

$$\delta \mathcal{F}_{\mathcal{E}}^{(K)} \equiv \mathcal{F}_{\mathcal{E}}^{(K)} / \mathcal{F}_{\text{Haar}}^{(K)} - 1 \leq \epsilon, \quad (3)$$

and one can show that the relative deviation is in fact equivalent to the definition by the normalized moment distance (cf. Appendix A).

Previous studies on the conventional DT [4–6] (cf. Fig. 1a) focused on the projected ensemble obtained from a single fixed unitary on a trivial initial state. It requires  $N_B = \Omega(K N_A + \log(1/\epsilon))$  bath qubits to achieve the  $\epsilon$ -approximate  $K$ -design [4], which creates an overhead growing with the system size and especially for high-order state design generation.

Inspired by the quantum circuit layout of Ref. [14], we propose the holographic deep thermalization (HDT) (cf. Fig. 1b), which extends the time direction to  $T$  discrete steps to compensate for the reduction in space resource—in the same spirit of holographic quantum simulation [13]. The HDT also begins with a trivial state, e.g.,  $|\psi_0\rangle = |0\rangle^{\otimes N_A}$ . In each of the  $T$  time steps,  $N_B$  bath qubits initialized in  $|0\rangle^{\otimes N_B}$  interact with data system  $A$  through a chaotic unitary  $U_t$ , which can be implemented by either a randomly sampled fixed quantum circuit [15, 16] or chaotic Hamiltonian evolution [4, 5]. Following projective measurements on the bath system, the *projected ensemble*  $\mathcal{E}_t$  of the data system at step  $t$  is fed towards the next time step as input.

*Convergence toward Haar ensemble.*— Assuming that each  $U_t$  is a fixed unitary sampled from Haar measure, one expects the *projected ensemble*  $\mathcal{E}_t$  to converge towards the fixed point of Haar random, as  $T$  increases. Below, we evaluate the frame potential to quantify the rate of convergence. As ensemble average results represent typical random unitaries with fluctuations suppressed by system size and self-averaging over time, we consider the expected frame-potential averaged over all  $\{U_t\}$  in the same spirit of Refs. [4–6]. Denoting the data and bath system dimension as  $d_A = 2^{N_A}$  and  $d_B = 2^{N_B}$ , we begin with exact solution for the first-order frame potential.

**Theorem 1** *The expected first-order frame potential  $\mathcal{F}^{(1)}(t)$  of the projected ensemble  $\mathcal{E}_t$  at step  $t$  in the holographic deep thermalization is*

$$\mathbb{E}_{\text{Haar}} \mathcal{F}^{(1)}(t) = \frac{d_A^2 (d_B + 1)}{d_A^2 d_B + 1} \mathcal{F}_{\text{Haar}}^{(1)} + \frac{(d_A - 1)(d_A d_B - 1)}{d_A^2 d_B + 1} \left( \frac{(d_A^2 - 1) d_B}{d_A^2 d_B^2 - 1} \right)^t. \quad (4)$$

*In the thermodynamic limit of data system  $d_A \rightarrow \infty$ ,*

$$\mathbb{E}_{\text{Haar}} \mathcal{F}^{(1)}(t) \simeq (1 + 1/d_B) \mathcal{F}_{\text{Haar}}^{(1)} + d_B^{-t}. \quad (5)$$

We present the proof in Appendix B and numerically verify Eq. (4) in Fig. 2ab, where a perfect agreement is found. In addition, we also perform noisy simulation for IBM quantum devices, with a size  $N_A = 2$  and  $N_B = 1$  up to  $t = 8$  steps, where a good agreement is found up to some additional decay from noise (see Appendix).

For higher-order moments, we have the following asymptotic lower bound.

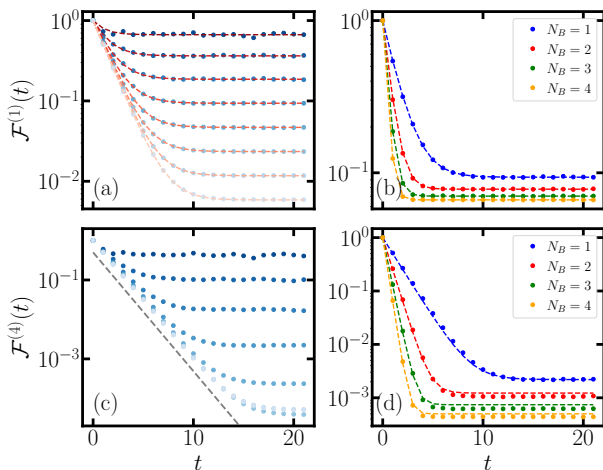


Figure 2. Dynamics of frame potential  $\mathcal{F}^{(K)}$  with  $K = 1$  (top) and  $K = 4$  (bottom). In the left panel (a)(c), the bath size is  $N_B = 1$ . Blue dots from dark to light represent numerical simulation results with system size  $N_A = 1, \dots, 8$ . In the right panel (b)(d), the system size is  $N_A = 4$ . Color dots represent numerical simulation results with bath size  $N_B = 1, \dots, 4$ . Red dashed lines (from dark to light) in (a) and colored dashed lines in (b) represent theoretical prediction of Eq. (4) in Theorem 1. The Grey dashed line in (c) shows the scaling of convergence  $\sim d_B^{-t}$ . Note that the overlapping dots for small frame potential is due to finite sampling error. Colored dashed lines in (d) represent Eq. (7).

**Lemma 2** *The expected  $K$ -th frame potential  $\mathcal{F}^{(K)}(t)$  ( $K > 1$ ) of the projected ensemble  $\mathcal{E}_t$  at step  $t$  in the holographic deep thermalization has an asymptotic lower bound ( $d_A \gg 1$ )*

$$\mathbb{E}_{\text{Haar}} \mathcal{F}^{(K)}(t) \gtrsim \left( \frac{d_A^2 d_B}{d_A^2 d_B^2 - 1} \right)^t \simeq \left( \frac{1}{d_B} \right)^t. \quad (6)$$

Besides the above rigorous lower bound, we also provide an empirical result at the same limit of  $d_A \gg 1$ ,

$$\mathbb{E}_{\text{Haar}} \mathcal{F}^{(K)}(t) \simeq d_B^{-t} + (1 + (2^K - 1)/d_B) \mathcal{F}_{\text{Haar}}^{(K)}. \quad (7)$$

While the specific constant term combines numerical observation and the analytical result for  $K = 1$  in Eq. (5), the form of the solution in Eq. (7) can be obtained under reasonable assumptions, as we present in Appendix B.

We provide numerical evidence to support Eq. (7). In Fig. 2c, for a fixed bath size  $N_B$ , the convergence of higher-order frame potentials also demonstrates the rate of  $1/d_B$  (gray dashed line), independent of either data system size  $N_A$  or order  $K$ . In Fig. 2d, the dynamical solution in Eq. (7) aligns with the numerical results and thus well describes the convergence dynamics of higher-order frame potential with  $K > 1$ . We further show the relative deviation of converged frame potential  $\delta\mathcal{F}^{(K)}(\infty) = \mathcal{F}^{(K)}(\infty)/\mathcal{F}_{\text{Haar}}^{(K)} - 1$  versus  $N_A$  and  $N_B$ , which is a direct measure on the approximation error to  $K$ -design. In Fig. 3a, given a bath of  $N_B$

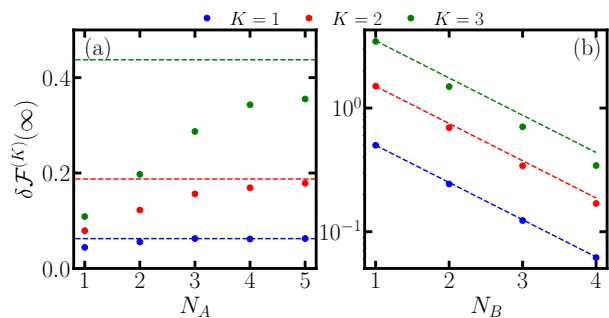


Figure 3. Relative deviation of converged frame potential  $\delta\mathcal{F}^{(K)}(\infty) = \mathcal{F}^{(K)}(\infty)/\mathcal{F}_{\text{Haar}}^{(K)} - 1$ . The system consists of (a)  $N_B = 4$  bath qubits with various  $N_A$  data qubits and (b)  $N_A = 4$  data qubits with various  $N_B$  bath qubits. Dots represents numerical simulation results and dashed lines represent theoretical prediction in Eq. (4) (blue) and Eq. (7) (red and green) as  $(2^K - 1)/d_B$ .

qubits, the relative deviation (dots) saturates towards a constant (dashed lines) independent of data system size  $N_A$ , though increases with  $K$  due to stronger randomness necessities. Meanwhile, increasing the bath system size can reduce the deviation exponentially in Fig. 3b as we have seen in Fig. 2bd.

*Space-time trade-off.*—Here, we analyze the space-time trade-off from Theorem 1 for  $K = 1$  and Eq. (7) for  $K \geq 1$  in details, assuming that each unitary  $U_t$  is implemented via a gate-based local quantum circuit. Generating an  $\epsilon$ -approximate  $K$ -design state ensemble requires  $\mathbb{E}_{\text{Haar}} \mathcal{F}^{(K)}(\infty) \leq (1 + \epsilon)\mathcal{F}_{\text{Haar}}^{(K)}$ , thus  $(2^K - 1)/d_B \lesssim \epsilon$ —only a constant number of  $N_B \gtrsim K + \log_2(1/\epsilon)$  bath qubits provided large data system as  $d_A \gg 1$ . Now assume that  $N_B \gtrsim K + \log_2(1/\epsilon)$  so that the long-time error  $\mathbb{E}_{\text{Haar}} \mathcal{F}^{(K)}(\infty)/\mathcal{F}_{\text{Haar}}^{(K)} - 1 \leq \epsilon/2$ . Then the residual error due to convergence in a finite  $T$  steps must be at most  $\epsilon/2$  to achieve an  $\epsilon$ -approximate  $K$ -design for the Haar random ensemble. As the convergence speed toward  $K$ -design is  $d_B^{-t}$  regardless of order  $K$ , the necessary number of time steps for convergence in  $K$ -th order becomes

$$T \times N_B \gtrsim KN_A - \log_2(K!) + \log_2\left(\frac{1}{\epsilon}\right), \quad (8)$$

leading to the trade-off between space—the number of ancilla  $N_B$ —and time step  $T$ , hence the name ‘holographic deep thermalization’. To reach the same performance on  $N_A$  qubits, the time-space product  $T \times N_B$  is roughly constant. Note that conventional DT corresponding to  $T = 1$ , requires bath size  $N_B \gtrsim KN_A + \log_2(1/\epsilon)$ , compared to the minimum constant number ancillae  $N_B \gtrsim K + \log_2(1/\epsilon)$  in the HDT.

In a gate-based realization of HDT, each unitary  $U_t$  requires  $\propto (N_A + N_B)$  layers of quantum gates in order to represent a fixed Haar-randomly-sampled unitary. Therefore, a more comprehensive way of quantifying the resource is via the quantum circuit size, which roughly

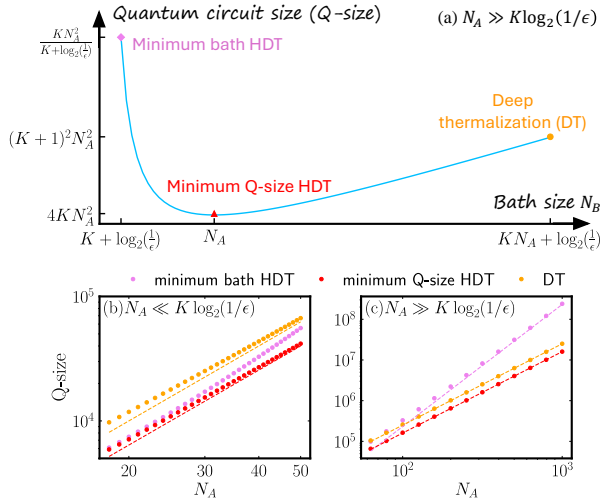


Figure 4. Quantum circuit size (Q-size) of HDT in generating  $\epsilon$ -approximate  $K$ -design. We plot the Q-size versus bath size in (a) for large system  $N_A \gg K \log_2(1/\epsilon)$  assuming  $K < \log_2(1/\epsilon)$ . Orange circle represent conventional DT, which also corresponds to  $T = 1$  in HDT. Red triangle and violet diamond represent Q-size in HDT with minimum Q-size and minimum bath separately. The labels on  $y$ -axis represent the scaling of Q-size from Eq. (10). In (b) and (c), we plot Q-size versus system size  $N_A$  for small and large system with bath size chosen specified in (a) with  $K = 4$  and  $\epsilon = 10^{-4}$ , namely  $N_B = 17, N_A, 4N_A + 13$  for minimum bath HDT, minimum Q-size HDT and conventional DT. Dots are numerically solved and dashed lines are the scaling indicated in (a).

equals the total number of gates. From Ineq. (8), we have the leading-order overall quantum circuit size (Q-size),

$$\begin{aligned} \text{Q-size} &\equiv \text{depth per step} \times T \times (N_A + N_B) \\ &\propto (N_A + N_B) \left( \frac{N_A}{N_B} + 1 \right) \left[ KN_A - \log_2(K!) + \log_2\left(\frac{1}{\epsilon}\right) \right]. \end{aligned} \quad (9)$$

$$(10)$$

Below, we provide a detailed analysis on the quantum circuit size, assuming that  $K < \log_2(1/\epsilon)$  and  $N_A \gg 1$ , while we leave the discussion of the other case in Appendix C. As summarized schematically in Fig. 4a, for large system  $N_A \gg K \log_2(1/\epsilon)$ , the minimum quantum circuit size Q-size  $\propto 4KN_A^2$  is achieved at  $N_B = N_A$ , as indicated by the red triangle. Meanwhile, in conventional DT corresponding to  $T = 1$  with  $N_B = KN_A + \log_2(1/\epsilon)$ , we have Q-size  $\propto (K+1)^2 N_A^2$ , as indicated by the orange dot. For the minimum space (bath) case of  $N_B \sim K + \log_2(1/\epsilon)$ , the quantum circuit size grows as  $KN_A^3 / (K + \log_2(1/\epsilon))$ . The above scalings (dashed lines) agree with numerics (dots) in Fig. 4c. On the other hand, for relative small system  $N_A \ll K \log_2(1/\epsilon)$ , the minimum Q-size (red) and conventional DT (orange) remain quadratic growth with  $N_A$ , shown Fig. 4b. However, the minimum bath case (violet) undergoes a continuous transition from quadratic toward cubic growth and remains smaller necessary resources compared to conven-

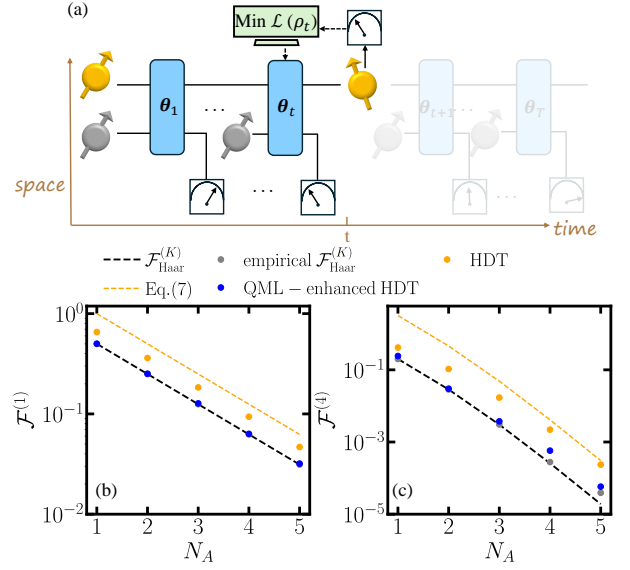


Figure 5. QML-enhanced HDT. In (a), we show the conceptual plot of the training process. In (b) and (c), we show the frame potential for  $K = 1$  and  $K = 4$  of output state ensemble. Orange dots represent converged frame potential in HDT with random unitary implementation. Orange dashed line is the theoretical prediction in Eq. (7). Blue dots are frame potential of output state ensemble from QML-enhanced HDT. Black dashed line and gray dots show the exact and empirical of Haar ensemble frame potential.

tional DT.

*Quantum machine learning enhancement.*— The task of random quantum state generation can be considered as a Dirac- $\delta$  distributed ensemble of a single initial state towards a Haar ensemble of states. In this regard, we can further enhance HDT via generative QML [14]. As shown in Fig. 5a, the unitary at time step  $t$  is a parameterized unitary  $U(\theta_t)$ . We optimize the parameters  $\{\theta_t\}_{t=1}^T$  to obtain the best Haar random ensemble at the output.

Towards this goal, we consider a divide-and-conquer strategy of only training the unitary  $U(\theta_t)$  in the  $t$ th training step, via minimizing a loss function  $\mathcal{L}_t(\mathcal{E}_t)$  on the state ensemble  $\mathcal{E}_t$ . While a greedy strategy may hope for  $\mathcal{E}_t$  to be close to Haar random ensemble  $\mathcal{E}_{\text{Haar}}$  at each training step, we take a less cost function  $\mathcal{L}_t(\mathcal{E}_t) = (1 - \tau_t)D(\mathcal{E}_t, |\psi_0\rangle) + \tau_t D(\mathcal{E}_t, \mathcal{E}_{\text{Haar}})$  as an interpolation of ‘distances’ to the initial single-state ensemble  $|\psi_0\rangle$  and Haar ensemble, with a monotonically increasing scheduling function  $\tau_t \in [0, 1]$ . Here  $D(\cdot, \cdot)$  characterize the ‘distance’ between two ensembles (see Appendix). To enable efficient evaluation of the loss function on actual quantum devices, we consider the most simple choice of ‘distance’  $D(\cdot, \cdot)$ , the super-fidelity between the average state  $\rho_t = \mathbb{E}_{\phi \sim \mathcal{E}_t} |\phi\rangle\langle\phi|$  of the ensembles—only keeping the first-moment information. We expect that the final generated state ensemble  $\mathcal{E}_T$  is still able to capture some of the higher moment property of true Haar ensemble

with large enough number of steps  $T$  thus sufficient randomness from measurements.

We numerically simulate the training of the QML-enhanced HDT with  $T = 32$  and  $N_B = 1$  and the results are presented in Fig. 5bc, where QML-enhanced frame potential (blue dots) lies very close to the exact Haar value (black dashed), up to deviations caused by finite sample indicated by the finite-sample of Haar results (gray dots). Constant advantage over the untrained HDT is obtained via the QML enhancement. Details of the quantum circuit ansatz and training are provided in Appendix.

*Discussion.*— While Ref. [17] proposes to inject classical randomness to enhance DT to save resource; our approach allows the trade-off of space and time, without relying on any classical randomness. We point out some future directions. The rigorous proof for the dynamics of higher-order frame potential is subject to a future study for a complete theoretical understanding. It is an interesting open question to explore the thermalization dynamics in HDT with other types of unitaries, such as the dual unitary [5, 6] and constrained systems like quantum many-body scar where the eigenstate thermalization hypothesis (ETH) is weakly broken [18].

We focused on the Haar random unitary ensemble in this work, equivalent to the infinite temperature scenario for typical chaotic Hamiltonian evolution where we expect the same dynamics occurs. For a finite temperature, it remains open to study whether the HDT can lead to the same Scrooge ensemble, as recently found in the conventional DT [19].

Our model can also be regarded as a generalized monitored circuit with fixed measurement rate and location, thus paving the way toward a comprehensive understanding of complexity growth in the monitored circuit beyond entanglement growth transition [20]. Finally, the step-wise scrambling property of HDT makes also suitable to replace the forward scrambling circuit in QuDDPM [14], avoiding the need of classical randomness.

*Acknowledgments.*— QZ and BZ acknowledge support from NSF (CCF-2240641, OMA-2326746, 2350153) and ONR N00014-23-1-2296. XC and PX acknowledge support from NSF (DMS-2413404, 2347760). This work was partially funded by an unrestricted gift from Google and a gift from the Simons Foundation. Part of the research was conducted using IBM Quantum Systems provided through USC’s IBM Quantum Innovation Center.

*Appendix on moments.*— Statistical properties of the projected ensemble  $\mathcal{E}(\Psi)$  are characterized by its  $K$ -th moment ( $K \geq 1$ ), which is captured by the  $K$ -th moment operator of ensemble [1, 4–6],

$$\rho_{\mathcal{E}}^{(K)} = \sum_z p_z (|\psi_z\rangle\langle\psi_z|)^{\otimes K}. \quad (11)$$

Specifically, for Haar ensemble in Hilbert space of dimen-

sion  $d_A$ ,  $\rho_{\text{Haar}}^{(K)}$  can be analytically written as

$$\rho_{\text{Haar}}^{(K)} = \frac{\sum_{\pi \in S_K} \hat{\pi}}{\prod_{i=0}^{K-1} (d_A + i)} = \frac{\Pi_K}{\binom{K+d_A-1}{d_A-1}}, \quad (12)$$

where  $S_K$  is the symmetric group on  $K$  element set,  $\hat{\pi}$  is the operator representation of permutation on  $\mathcal{H}^{\otimes K}$ , and  $\Pi_K = \sum_{\pi \in S_K} \hat{\pi}/K!$  is the projector onto the symmetric subspace.

While in the main text, we adopted the frame potential to quantify the closeness to Haar state ensemble, which can be shown to also equal the purity of the moment,  $\mathcal{F}_{\mathcal{E}}^{(K)} = \text{tr}[\rho_{\mathcal{E}}^{(K)2}]$ . One can show that the relative deviation is in fact equivalent to the normalized moment distance with  $\|\cdot\|_2$  denoting Schatten-2 norm

$$\sqrt{\delta\mathcal{F}_{\mathcal{E}}^{(K)}} = \Delta_{\mathcal{E}}^{(K)} \equiv \left\| \rho_{\mathcal{E}}^{(K)} - \rho_{\text{Haar}}^{(K)} \right\|_2 / \left\| \rho_{\text{Haar}}^{(K)} \right\|_2. \quad (13)$$

*Appendix on QML.*— We have chosen the loss function

$$\mathcal{L}_t(\rho_t) = (1 - \tau_t)(1 - F_{\text{sup}}(\rho_t, |\psi_0\rangle)) + \tau_t(1 - F_{\text{sup}}(\rho_t, \mathbf{I}/d_A)), \quad (14)$$

where  $\rho_t$  is the average state at step  $t$  and  $\mathbf{I}/d_A$  is the maximally mixed state on the  $N_A$  data qubit. We adopt the *superfidelity* [21] for efficient evaluation in training without significant impact on performance

$$F_{\text{sup}}(\rho, \sigma) = \text{tr}(\rho\sigma) + \sqrt{(1 - \text{tr}\rho^2)(1 - \text{tr}\sigma^2)}. \quad (15)$$

Specifically, for the two states  $|\psi_0\rangle$  and  $\mathbf{I}/d_A$  considered in loss function, the *superfidelity* can be further simplified to  $F_{\text{sup}}(\rho_t, |\psi_0\rangle) = \langle\psi_0|\rho_t|\psi_0\rangle$  and  $F_{\text{sup}}(\rho_t, \mathbf{I}/2^N) = 1/d_A + \sqrt{(d_A - 1)(1 - \text{tr}\rho_t^2)/d_A}$ . Therefore, one can regard the loss function in Eq. (14) as a nonlinear scheduling on the decay of purity of  $\rho_t$  towards  $1/d_A$ . The loss function considered here is also closed connected to the MMD distance in QuDDPM [14].

Note that utilizing the average-state-dependent loss function avoids the precise control and tracking of measurement results on ancillary qubits, though a Monte-Carlo sampling error exists due to finite sampling. In particular, both  $\langle\psi_0|\rho_t|\psi_0\rangle$  and  $\text{tr}(\rho_t^2)$  are experimental tractable to measure. For the purity measure, one can either run two quantum devices simultaneously to obtain two copies of the average state, and then estimate the purity via a control-SWAP circuit with an extra control qubit. Another recent proposed option relies on the random measurement toolbox, e.g., classical shadow [8]. For the control-SWAP circuit, it requires the application of a global control-SWAP gate on the two copies of  $N$ -qubit state conditioned on control qubit’s state, which can be decomposed into  $N$  control-SWAP gates applied on two qubits only. In comparison, classical shadow only requires an extra layer of random single qubit Pauli gate for efficient estimation, though at the cost of more random measurements.

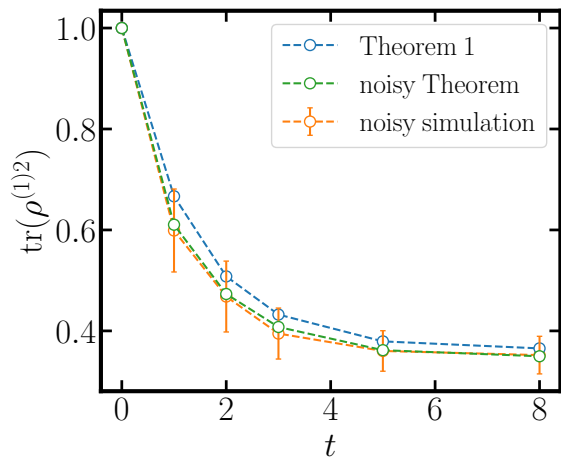


Figure 6. Dynamics of average state purity in noisy simulation. Blue dots represent theoretical prediction from Theorem 1. Green dots represents Theorem 1 with noise model, detailed in Appendix. E. Orange dots with errorbar represent noisy simulation results for IBM Kyiv.

In each step, we parameterize the unitary via a hardware-efficient ansatz [22] where each layer of circuit involves single qubit X and Y rotations followed by control-Z gates in brickwall fashion. In numerical simulation, we choose  $L = 2(N_A + N_B)$  layers for each step.

*Appendix on noisy simulation.*— We validate the dynamics of frame potential in HDT through noisy simulations of experiments on IBM Quantum. The noisy simulations utilize noise model for the hardware IBM Kyiv provided by Qiskit [23]. To achieve a sufficient random and complex unitary in each step, we implement HEA [22] and randomly initialize its parameters. We consider a system of  $N_A = 2$  and  $N_B = 1$  qubits, and in each step, the circuit involves  $L = 5$  layers. For a purpose of validation, we implement the mid-circuit measurements and resets by equivalently expanding the bath system and

postponing all measurements to the end. To evaluate the first-order frame potential, we perform measurement on the data system over all Pauli basis to obtain

$$\text{tr}(\rho^{(1)2}) = \frac{1}{d} \sum_{P \in \mathcal{P}_{N_A}} \text{tr}(\rho^{(1)}P)^2, \quad (16)$$

where  $\mathcal{P}_{N_A}$  is the Pauli group on  $N_A$  qubits omitting phases and  $\rho^{(1)}$  is the moment ensemble defined in Eq. (11). For large data system, one can perform classical shadow [8] for an efficient estimation on the purity.

In Fig. 6, we present noisy simulation results (orange) and compare it to theoretical prediction (blue) in Eq. (4) of Theorem 1. In noisy simulation, we average over 500 different initial parameters of HEA, and perform 1000 shots for each Pauli expectation. The decay of purity (orange) in noisy simulation is characterized by our theory (blue), indicating the convergence toward Haar ensemble in first moment through HDT. The gap between the noisy simulation and ideal theory is due to the hardware noise. To fulfill the gap, we further provide a noise-corrected theory (green), detailed in Appendix. E and it aligns with simulation result.

*Appendix on numerical details.*— Fig. 2: Each dots is an average over 50 Haar unitary realizations with ensemble of  $5 \times 10^4$  samples for  $N_A = 1, \dots, 6$  and 20 Haar unitaries realizations with ensemble size of  $2 \times 10^4$  samples for  $N_A = 7, 8$ .

Fig. 3: Each dot is an average over 50 Haar unitaries realizations with ensemble of  $5 \times 10^4$  samples at step  $T = 32$ . Here we take the empirical  $\mathcal{F}_{\text{Haar}}^{(K)}$  by averaging over 50 ensembles of  $5 \times 10^4$  Haar random states to reduce the finite size effect.

Fig. 5: In holographic deep thermalization with random unitary implementation, we average over 50 Haar unitaries realizations with ensemble of  $5 \times 10^4$  samples. In QML-enhanced holographic deep thermalization, we average over 20 post-measurement ensembles, each of which includes  $5 \times 10^4$  samples. The empirical  $\mathcal{F}_{\text{Haar}}^{(K)}$  is averaged over 50 ensembles of  $5 \times 10^4$  Haar random states.

- 
- [1] D. A. Roberts and B. Yoshida, Journal of High Energy Physics **2017**, 1 (2017).  
[2] J. R. McClean, S. Boixo, V. N. Smelyanskiy, R. Babbush, and H. Neven, Nat. Commun. **9**, 4812 (2018).  
[3] M. Cerezo, A. Sone, T. Volkoff, L. Cincio, and P. J. Coles, Nat. Commun. **12**, 1791 (2021).  
[4] J. S. Cotler, D. K. Mark, H.-Y. Huang, F. Hernandez, J. Choi, A. L. Shaw, M. Endres, and S. Choi, PRX quantum **4**, 010311 (2023).  
[5] W. W. Ho and S. Choi, Physical Review Letters **128**, 060601 (2022).  
[6] M. Ippoliti and W. W. Ho, PRX Quantum **4**, 030322 (2023).  
[7] S. Pirandola, U. L. Andersen, L. Banchi, M. Berta, D. Bunandar, R. Colbeck, D. Englund, T. Gehring, C. Lupo, C. Ottaviani, *et al.*, Advances in optics and photonics **12**, 1012 (2020).  
[8] H.-Y. Huang, R. Kueng, and J. Preskill, Nature Physics **16**, 1050 (2020).  
[9] A. Elben, S. T. Flammia, H.-Y. Huang, R. Kueng, J. Preskill, B. Vermersch, and P. Zoller, Nature Reviews Physics **5**, 9 (2023).  
[10] F. G. Brandao, A. W. Harrow, and M. Horodecki, Communications in Mathematical Physics **346**, 397 (2016).  
[11] A. W. Harrow and S. Mehraban, Communications in Mathematical Physics, 1 (2023).  
[12] J. Choi, A. L. Shaw, I. S. Madjarov, X. Xie, R. Finkelstein, J. P. Covey, J. S. Cotler, D. K. Mark, H.-Y. Huang, A. Kale, *et al.*, Nature **613**, 468 (2023).  
[13] S. Anand, J. Hauschild, Y. Zhang, A. C. Potter, and

- M. P. Zaletel, PRX Quantum **4**, 030334 (2023).
- [14] B. Zhang, P. Xu, X. Chen, and Q. Zhuang, Physical Review Letters **132**, 100602 (2024).
- [15] A. Nahum, J. Ruhman, S. Vijay, and J. Haah, Physical Review X **7**, 031016 (2017).
- [16] A. Nahum, S. Vijay, and J. Haah, Physical Review X **8**, 021014 (2018).
- [17] W.-K. Mok, T. Haug, A. L. Shaw, M. Endres, and J. Preskill, arXiv:2410.05181 (2024).
- [18] T. Bhore, J.-Y. Desaulles, and Z. Papić, Physical Review B **108**, 104317 (2023).
- [19] D. K. Mark, F. Surace, A. Elben, A. L. Shaw, J. Choi, G. Refael, M. Endres, and S. Choi, arXiv preprint arXiv:2403.11970 (2024).
- [20] B. Skinner, J. Ruhman, and A. Nahum, Physical Review X **9**, 031009 (2019).
- [21] M. Cerezo, A. Sone, J. L. Beckey, and P. J. Coles, Quantum Science and Technology **6**, 035008 (2021).
- [22] A. Kandala, A. Mezzacapo, K. Temme, M. Takita, M. Brink, J. M. Chow, and J. M. Gambetta, nature **549**, 242 (2017).
- [23] Qiskit contributors, Qiskit: An open-source framework for quantum computing (2023).
- [24] M. Ippoliti and W. W. Ho, Quantum **6**, 886 (2022).
- [25] P. W. Claeys and A. Lamacraft, Quantum **6**, 738 (2022).
- [26] F. G. Brandão, A. Kalev, T. Li, C. Y.-Y. Lin, K. M. Svore, and X. Wu, arXiv:1710.02581 (2017).
- [27] S.-X. Zhang, J. Allcock, Z.-Q. Wan, S. Liu, J. Sun, H. Yu, X.-H. Yang, J. Qiu, Z. Ye, Y.-Q. Chen, *et al.*, Quantum **7**, 912 (2023).
- [28] V. Bergholm, J. Izaac, M. Schuld, C. Gogolin, S. Ahmed, V. Ajith, M. S. Alam, G. Alonso-Linaje, B. AkashNarayanan, A. Asadi, *et al.*, arXiv preprint arXiv:1811.04968 (2018).

## Appendix A: Preliminary

To quantify the approximation of an arbitrary state ensemble  $\mathcal{E}$  to Haar ensemble ( $K$ -design), we consider the (normalized)  $p$ -order moment distance and the relative deviation of frame potential as [6]

$$\Delta_{\mathcal{E},p}^{(K)} = \frac{\left\| \rho_{\mathcal{E}}^{(K)} - \rho_{\text{Haar}}^{(K)} \right\|_p}{\left\| \rho_{\text{Haar}}^{(K)} \right\|_p}, \quad (\text{A1})$$

$$\delta \mathcal{F}_{\mathcal{E}}^{(K)} = \frac{\mathcal{F}_{\mathcal{E}}^{(K)}}{\mathcal{F}_{\text{Haar}}^{(K)}} - 1, \quad (\text{A2})$$

where  $\|\cdot\|_p$  is the  $p$ -Schatten norm and  $\rho_{\mathcal{E}}^{(K)}$  is defined in Eq. (11). Commonly used order of norms include  $p = 1$  (trace norm),  $p = 2$  (Frobenius norm) and  $p = \infty$  (operator norm). Note that  $\left\| \rho_{\text{Haar}}^{(K)} \right\|_1 = 1$ , then

$$\Delta_{\mathcal{E},1}^{(K)} = \left\| \rho_{\mathcal{E}}^{(K)} - \rho_{\text{Haar}}^{(K)} \right\|_1 = 2D_{\text{tr}} \left( \rho_{\mathcal{E}}^{(K)}, \rho_{\text{Haar}}^{(K)} \right), \quad (\text{A3})$$

which is equivalent to trace distance between  $K$ -th-moment of  $\mathcal{E}$  and Haar, widely explored in Refs. [4, 5]. We can also show that for  $p = 2$ , it is equivalent to the frame potential as [6]

$$\Delta_{\mathcal{E},2}^{(K)} = \frac{\left\| \rho_{\mathcal{E}}^{(K)} - \rho_{\text{Haar}}^{(K)} \right\|_2}{\left\| \rho_{\text{Haar}}^{(K)} \right\|_2} \quad (\text{A4})$$

$$= \frac{\text{tr} \left[ \left( \rho_{\mathcal{E}}^{(K)} - \rho_{\text{Haar}}^{(K)} \right)^2 \right]^{1/2}}{\text{tr} \left[ \left( \rho_{\text{Haar}}^{(K)} \right)^2 \right]^{1/2}} \quad (\text{A5})$$

$$= \left( \frac{\mathcal{F}_{\mathcal{E}}^{(K)} - \mathcal{F}_{\text{Haar}}^{(K)}}{\mathcal{F}_{\text{Haar}}^{(K)}} \right)^{1/2} = \sqrt{\delta \mathcal{F}_{\mathcal{E}}^{(K)}}, \quad (\text{A6})$$

where we utilize  $\text{tr} \left( \rho_{\mathcal{E}}^{(K)} \rho_{\text{Haar}}^{(K)} \right) = \mathcal{F}_{\text{Haar}}^{(K)}$  in the third line. The norm with  $p = 1$  can also be bounded by  $p = 2$  norm with norm inequalities, therefore we mainly focus on the frame potential in the main text.

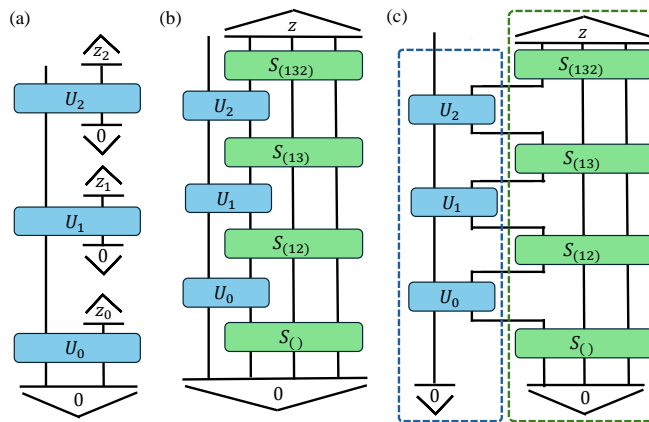


Figure 7. (a) Circuit diagram of holographic deep thermalization. Data and bath subsystems are both initialized in  $|0\rangle$ , evolved by a chaotic Hamiltonian, and followed by projective measurements and reset on bath. In (b), we show the equivalent circuit diagram by postponing projective measurements to the end. Here  $S_\pi$  represents the permutation operator of  $\pi$ , e.g.  $S_{(12)}$  represents the swap between  $B_1, B_2$ . In (c), we split the circuit in (b) into two parts, separated by a “temporal” cut. A state  $|\phi_z\rangle$  on “temporal” cut produced by the map (green box) is taken as the input into the linear map (blue box) in the left, and outputs the post-measurement on subsystem  $A$ . Here we plot the system of three steps.

## Appendix B: Dynamics of frame potential in holographic deep thermalization

In this section, we derive the frame potential dynamics in the holographic deep thermalization. Without losing generality, we model each unitary evolution  $U_t$  as a random unitary sampled from the Haar group  $\mathcal{U}_H$ . At step  $t$  in the holographic deep thermalization model, the input involves two parts, the data and bath side with qubits  $N_A, N_B$  thus dimension  $d_A = 2^{N_A}, d_B = 2^{N_B}$ . The derivation follows the notation conventions in Ref. [24]. Before doing the detailed calculation, we would like to clarify we are calculating the frame potential—purity of  $K$ -th moment state  $\rho^{(K)}$ —and then take the average; Taking an average first over the state will not lead to typical case results of a fixed sequence of unitaries. Indeed, the average state becomes fully mixed even just with a single step.

For the holographic deep thermalization shown in Fig. 7a, the joint system of  $A, B$  is initialized at  $|0\rangle$ , and in step  $t$ , we apply a Haar random unitary  $U_{t-1}$  on the joint system, followed by projective measurement and reset on  $B$ . Equivalently, we can postpone all mid-circuit measurements to the end of the circuit evolution while expanding the bath system to  $B \rightarrow B_1, \dots, B_T$  shown in Fig. 7b. Here the  $S_\pi$  represents the permutation operation of  $\pi$  on the expanded bath. We can further split the circuit into two parts by a “temporal cut”  $C$  (see Fig. 7c), which enables us an analytical analysis on the dynamics through the replica trick. The right block (enclosed by green dashed box) provides the  $d_B^{2T}$ -dimensional state  $|\phi_z\rangle = \otimes_{t=0}^{T-1} |0\rangle |z_t\rangle$  on the “time bond”. The left block (enclosed by blue dashed box), can thus be regarded as a linear map  $E$  applied on the “time bond” space and map it to subsystem  $A$ . The linear map can be explicitly written as

$$E_{a,c} = \sum_{\alpha} \prod_{t=0}^{T-1} \langle \alpha_{t+1}, c_{2t+1} | U_t | \alpha_t, c_{2t} \rangle \delta_{\alpha_0, 0} \delta_{\alpha_T, a} | a \rangle \langle c_{2T-1} | \dots \langle c_0 |, \quad (\text{B1})$$

where  $a$  is the index on subsystem  $A$  and  $c$  is the index on the temporal cut. The *projected ensemble* on  $A$  at step  $T$  can then be written as

$$\mathcal{E}(T) = \{p_z = \langle \phi_z | E^\dagger E | \psi_z \rangle, |\psi_z\rangle = E |\phi_z\rangle / \sqrt{p_z}, z = 0, \dots, d_B^T - 1\}. \quad (\text{B2})$$

We derive the dynamics of frame potentials for  $\mathcal{E}(T)$  in the following.

### 1. First order frame potential dynamics

For  $K = 1$ , the first moment of ensemble  $\mathcal{E}(T)$  is

$$\rho_A^{(1)}(T) = \sum_z p_z |\psi_z\rangle \langle \psi_z| = \sum_z E |\phi_z\rangle \langle \phi_z| E^\dagger. \quad (\text{B3})$$



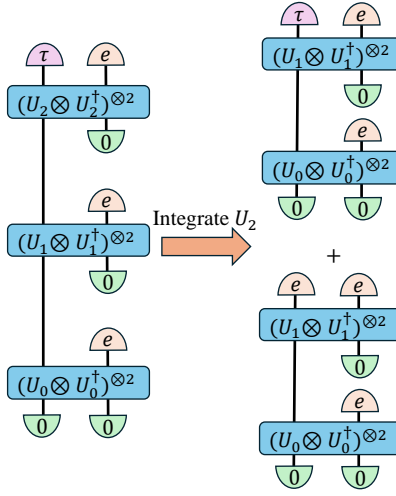


Figure 8. Tensor network representation of first-order frame potential. In the left we plot the case involving three steps. Each semi-circle represents the operator over two replicas. By integrating out the unitary  $U_2$  over Haar unitary group, we reach the two terms in the right (omitting coefficients). The boundary condition is either the same as the one before integration or trivial to be invariant under unitary evolution.

Note that

$$\sum_z |\phi_z\rangle\langle\phi_z| = \sum_z |z_{T-1}\rangle\langle z_{T-1}| \otimes |0\rangle\langle 0| \cdots |z_0\rangle\langle z_0| \otimes |0\rangle\langle 0| = (\mathbf{I} \otimes |0\rangle\langle 0|)^{\otimes T}, \quad (\text{B4})$$

where  $\mathbf{I}$  is the identity operation of dimension  $d_B$ . Therefore, the first moment becomes

$$\rho_A^{(1)}(T) = \sum_z E |\phi_z\rangle\langle\phi_z| E^\dagger \quad (\text{B5})$$

$$= E (\mathbf{I} \otimes |0\rangle\langle 0|)^{\otimes T} E^\dagger \quad (\text{B6})$$

$$= \sum_{\alpha, \alpha'} \sum_c \prod_{t=0}^{T-1} \langle \alpha_{t+1}, c_{2t+1} | U_t | \alpha_t, 0 \rangle \langle \alpha'_t, 0 | U_t^\dagger | \alpha'_{t+1}, c_{2t+1} \rangle \delta_{\alpha_0, 0} \delta_{\alpha'_0, 0} \delta_{\alpha_T, a} \delta_{\alpha'_T, a'} |a\rangle\langle a'| \quad (\text{B7})$$

$$= \sum_{\alpha, \alpha'} \prod_{t=0}^{T-1} \text{tr} \left( U_t (|\alpha_t\rangle\langle\alpha'_t|_A \otimes |0\rangle\langle 0|) U_t^\dagger |\alpha'_{t+1}\rangle\langle\alpha_{t+1}| \right) \delta_{\alpha_0, 0} \delta_{\alpha'_0, 0} \delta_{\alpha_T, a} \delta_{\alpha'_T, a'} |a\rangle\langle a'|. \quad (\text{B8})$$

From Eq. (2), the first-order frame potential is the purity of first moment as

$$\mathcal{F}^{(1)}(T) = \text{tr} \left( \rho_A^{(1)}(T)^2 \right) \quad (\text{B9})$$

$$\begin{aligned} &= \sum_{a, a'} \sum_{\alpha, \alpha', \beta, \beta'} \prod_{t=0}^{T-1} \text{tr} \left( U_t (|\alpha_t\rangle\langle\alpha'_t|_A \otimes |0\rangle\langle 0|) U_t^\dagger |\alpha'_{t+1}\rangle\langle\alpha_{t+1}| \right) \text{tr} \left( U_t (|\beta_t\rangle\langle\beta'_t|_A \otimes |0\rangle\langle 0|) U_t^\dagger |\beta'_{t+1}\rangle\langle\beta_{t+1}| \right) \\ &\quad \times \delta_{\alpha_0, 0} \delta_{\alpha'_0, 0} \delta_{\alpha_T, a} \delta_{\alpha'_T, a'} \delta_{\beta_0, 0} \delta_{\beta'_0, 0} \delta_{\beta_T, a'} \delta_{\beta'_T, a}. \end{aligned} \quad (\text{B10})$$

$$\begin{aligned} &= \sum_{a, a'} \sum_{\alpha, \alpha', \beta, \beta'} \prod_{t=0}^{T-1} \text{tr} \left( U_t^{\otimes 2} (|\alpha_t, \beta_t\rangle\langle\alpha'_t, \beta'_t|_A \otimes |0, 0\rangle\langle 0, 0|) U_t^{\dagger \otimes 2} |\alpha'_{t+1}, \beta'_{t+1}\rangle\langle\alpha_{t+1}, \beta_{t+1}| \right) \\ &\quad \times \delta_{\alpha_0, 0} \delta_{\alpha'_0, 0} \delta_{\alpha_T, a} \delta_{\alpha'_T, a'} \delta_{\beta_0, 0} \delta_{\beta'_0, 0} \delta_{\beta_T, a'} \delta_{\beta'_T, a}, \end{aligned} \quad (\text{B11})$$

which can be represented by a tensor diagram as in the left panel of Fig. 8, where the boundary condition is the transposition  $|\tau\rangle$  over two replicas in  $A$  and identity operator  $|e\rangle$ . Here we denote  $|A\rangle = \sum_{i,j} A_{i,j} |i\rangle |j\rangle$  as the vectorized operator following the convention in Ref. [24], and  $\langle A|B\rangle = \text{tr}(A^\dagger B)$ . We can now perform the Haar unitary ensemble average from  $U_{T-1}$  backwards to  $U_0$ . The unitary twirling channel over Haar random unitary [1] is

$$\mathbb{E}_{V \sim \mathcal{U}_{\text{Haar}}(d)} [V^{\otimes 2} \otimes V^{\dagger \otimes 2}] = \frac{1}{d^2 - 1} \left( |e\rangle\langle e| - \frac{1}{d} |e\rangle\langle\tau| + |\tau\rangle\langle\tau| - \frac{1}{d} |\tau\rangle\langle e| \right). \quad (\text{B12})$$

Therefore the ensemble average over  $U_{T-1}$  on boundary condition  $|\tau\rangle_A|e\rangle_B$  becomes

$$\mathbb{E}_{U_{T-1} \sim \mathcal{U}_{\text{Haar}}} \left[ U_{T-1}^{\otimes 2} \otimes U_{T-1}^{\dagger \otimes 2} \right] |\tau\rangle_A|e\rangle_B = \frac{1}{d_A^2 d_B^2 - 1} \left( |e\rangle\langle e| - \frac{1}{d} |e\rangle\langle \tau| + |\tau\rangle\langle \tau| - \frac{1}{d} |\tau\rangle\langle e| \right) |\tau\rangle_A|e\rangle_B \quad (\text{B13})$$

$$= \frac{1}{d_A^2 d_B^2 - 1} \left( \left[ (e|\tau\rangle_A d_B^2 - \frac{d_A^2 (\tau|e)_B}{d} \right] |e\rangle_A|e\rangle_B + \left[ d_A^2 (\tau|e)_B - \frac{(e|\tau)_A d_B^2}{d} \right] |\tau\rangle_A|\tau\rangle_B \right) \quad (\text{B14})$$

$$= \frac{d_B(d_A^2 - 1)}{d_A^2 d_B^2 - 1} |\tau\rangle_A|\tau\rangle_B + \frac{d_A(d_B^2 - 1)}{d_A^2 d_B^2 - 1} |e\rangle_A|e\rangle_B. \quad (\text{B15})$$

We then apply  $|e\rangle\langle 0|_B$  on subsystem  $B$  and have

$$|e\rangle\langle 0|_B \mathbb{E}_{U_{T-1} \sim \mathcal{U}_{\text{Haar}}} \left[ U_{T-1}^{\otimes 2} \otimes U_{T-1}^{\dagger \otimes 2} \right] |\tau\rangle_A|e\rangle_B = \frac{d_B(d_A^2 - 1)}{d_A^2 d_B^2 - 1} (0|\tau\rangle_B |\tau\rangle_A|e\rangle_B) + \frac{d_A(d_B^2 - 1)}{d_A^2 d_B^2 - 1} (0|e\rangle_B |e\rangle_A|e\rangle_B) \quad (\text{B16})$$

$$= \frac{d_B(d_A^2 - 1)}{d_A^2 d_B^2 - 1} |\tau\rangle_A|e\rangle_B + \frac{d_A(d_B^2 - 1)}{d_A^2 d_B^2 - 1} |e\rangle_A|e\rangle_B \quad (\text{B17})$$

where we utilize  $(0|\hat{\sigma})_B = 1$  for any permutation  $\sigma$ . The first and second part correspond to the right panel of Fig. 8. We see that the first part is the same boundary condition as in step  $T$ , while the second part remains invariant in the backward process. We are now ready to drive the recurrent equation for ensemble average frame potential as

$$\mathbb{E}_{\text{Haar}} \left[ \mathcal{F}^{(1)}(T) \right] = \frac{d_B(d_A^2 - 1)}{d_A^2 d_B^2 - 1} \mathbb{E}_{\text{Haar}} \left[ \mathcal{F}^{(1)}(T-1) \right] + \frac{d_A(d_B^2 - 1)}{d_A^2 d_B^2 - 1}, \quad (\text{B18})$$

with initial condition  $\mathbb{E}_{\text{Haar}} \left[ \mathcal{F}^{(1)}(0) \right] = 1$ . The recurrent equation can be analytically solved as

$$\mathbb{E}_{\text{Haar}} \left[ \mathcal{F}^{(1)}(t) \right] = \frac{(d_A - 1)(d_A d_B - 1)}{d_A^2 d_B + 1} \left( \frac{(d_A^2 - 1) d_B}{d_A^2 d_B^2 - 1} \right)^t + \frac{d_A^2 (d_B + 1)}{d_A^2 d_B + 1} \mathcal{F}_{\text{Haar}}^{(1)}, \quad (\text{B19})$$

where  $\mathcal{F}_{\text{H}}^{(1)} = 1/d_A$  is the first-order frame potential of Haar ensemble. In the thermodynamic limit of large number of data qubits  $d_A \rightarrow \infty$ , it can be reduced to

$$\mathbb{E}_{\mathcal{U}_{\text{H}}} \left[ \mathcal{F}^{(1)}(t) \right] = d_B^{-t} + \left( 1 + \frac{1}{d_B} \right) \mathcal{F}_{\text{H}}^{(1)}. \quad (\text{B20})$$

We also notice that it reproduces the known result in Ref. [4] by taking  $t = 1$ .

## 2. Higher order frame potential dynamics

In this part, we derive a phenomenological equation of the dynamics for higher-order frame potential. Following the ensemble (Eq. (B2)) at step  $T$ , the  $K$ -th moment is

$$\rho_A^{(K)}(T) = \sum_z p_z |\psi_z\rangle\langle\psi_z|^{\otimes K} \quad (\text{B21})$$

$$= \sum_z \langle\phi_z|E^\dagger E|\phi_z\rangle^{1-K} (E|\phi_z\rangle\langle\phi_z|E^\dagger)^{\otimes K}. \quad (\text{B22})$$

We utilize the replica-trick [25] as in other studies. We first define a pseudo moment

$$\rho_A^{(m,K)}(T) = \sum_z \langle\phi_z|E^\dagger E|\phi_z\rangle^m (E|\phi_z\rangle\langle\phi_z|E^\dagger)^{\otimes K} \quad (\text{B23})$$

$$= \text{tr}_{A_{1:m}} \left( \sum_z (E|\phi_z\rangle\langle\phi_z|E^\dagger)^{\otimes m+K} \right) \quad (\text{B24})$$

and take the limit  $m \rightarrow 1 - K$  at the end. In the last line we trace out the first  $m$  replicas. For convenience, we define  $r = m + K$ . Note that

$$\sum_z |\phi_z\rangle\langle\phi_z|^{\otimes r} = \sum_z \left( \otimes_{t=0}^{T-1} |z_t\rangle\langle z_t| \otimes |0\rangle\langle 0| \right)^{\otimes r} \quad (\text{B25})$$

$$= \sum_z \otimes_{t=0}^{T-1} |z_t^r\rangle\langle z_t^r| \otimes |0^r\rangle\langle 0^r| \quad (\text{B26})$$

$$= \otimes_{t=0}^{T-1} \left( \sum_{z_t} |z_t^r\rangle\langle z_t^r| \otimes |0^r\rangle\langle 0^r| \right) \quad (\text{B27})$$

$$= (D_r \otimes |0^r\rangle\langle 0^r|)^{\otimes T} \quad (\text{B28})$$

where for simplicity of notation, we denote  $|b^r\rangle = |b^{\otimes r}\rangle$ . Here  $D_r$  is the projector onto the space of  $r$  replicas. The pseudo moment operator then becomes

$$\rho_A^{(m,K)}(T) = \text{tr}_{A_{1:m}}(E^{\otimes r} (D_r \otimes |0^r\rangle\langle 0^r|)^{\otimes T} E^{\dagger \otimes r}), \quad (\text{B29})$$

and the psuedo frame potential is

$$\mathcal{F}^{(m,K)}(T) = \text{tr} \left( \rho_A^{(m,K)}(T)^2 \right) \quad (\text{B30})$$

$$= \text{tr} \left[ \text{tr}_{A_{1:m}}(E^{\otimes r} (D_r \otimes |r\rangle\langle r|)^{\otimes T} E^{\dagger \otimes r})^2 \right] \quad (\text{B31})$$

$$= \text{tr} \left( E^{\otimes 2r} (D_r^{\otimes 2} \otimes |0^{2r}\rangle\langle 0^{2r}|)^{\otimes T} E^{\dagger \otimes 2r} \right), \quad (\text{B32})$$

which indicates that it can also be written as in a tensor diagram similar to Fig. 8, where the boundary condition becomes  $D_r^{\otimes 2}$  on subsystem  $B$ , and transposition  $\tau$  over  $2K$  replicas only on subsystem  $A$ . For unitary twirling over  $r$  replicas, we have

$$\mathbb{E} \left[ (U \otimes U^\dagger)^{\otimes 2r} \right] = \sum_{\sigma, \pi \in S_{2r}} \text{Wg}(\sigma^{-1}\pi, 2r) |\hat{\sigma}\rangle\langle\hat{\pi}| \simeq \text{Wg}(e, 2r) \sum_{\sigma \in S_{2r}} |\hat{\sigma}\rangle\langle\hat{\sigma}|, \quad (\text{B33})$$

where  $S_{2r}$  is the permutation group over  $2r$  replicas, and  $\hat{\pi}$  is the operator representation of permutation  $\pi$ .  $\text{Wg}(\sigma^{-1}\pi, 2r)$  is the Weingarten coefficient defined to be  $\text{Wg}(\sigma^{-1}\pi, 2r) = \left( d^{|\sigma^{-1}\pi|} \right)^{-1}$  where  $|\sigma^{-1}\pi|$  denotes the number of cycles in the permutation  $\sigma^{-1}\pi$ . In the large dimension limit  $d \gg 1$ , we can only keep the leading order coefficient with  $\sigma = \pi$ , leading to the approximation. Following the same backward formalism, we start from the end as

$$|D_r^{\otimes 2}\rangle\langle 0^{2r}|_B \mathbb{E} \left[ (U \otimes U^\dagger)^{\otimes 2r} \right] |\tau\rangle_A |D_r^{\otimes 2}\rangle_B \quad (\text{B34})$$

$$\simeq \text{Wg}(e, 2r) |D_r^{\otimes 2}\rangle\langle 0^{2r}|_B \sum_{\sigma} (\sigma|\tau\rangle_A (\sigma|D_r^{\otimes 2}\rangle_B |\sigma\rangle_A |\sigma\rangle_B) \quad (\text{B35})$$

$$= \text{Wg}(e, 2r) (\tau|\tau\rangle_A (\tau|D_r^{\otimes 2}\rangle_B |0^{2r}\rangle_B |\tau\rangle_A |D_r^{\otimes 2}\rangle_B) + \text{Wg}(e, 2r) \sum_{\sigma \neq \tau} (\sigma|\tau\rangle_A (\sigma|D_r^{\otimes 2}\rangle_B |0^{2r}\rangle_B |\sigma\rangle_A |D_r^{\otimes 2}\rangle_B) \quad (\text{B36})$$

$$= \text{Wg}(e, 2r) d_A^{2r} (\tau|D_r^{\otimes 2}\rangle_B |\tau\rangle_A |D_r^{\otimes 2}\rangle_B) + \text{Wg}(e, 2r) \sum_{\sigma \neq \tau} (\sigma|\tau\rangle_A (\sigma|D_r^{\otimes 2}\rangle_B |\sigma\rangle_A |D_r^{\otimes 2}\rangle_B). \quad (\text{B37})$$

For an arbitrary  $\sigma \in S_{2r}$ , we have

$$(\sigma|D_2^{\otimes 2}\rangle_B) = \text{tr}(\sigma^\dagger D_2^{\otimes 2}) \quad (\text{B38})$$

$$= \sum_{z, z'} \langle z^r z'^r | \sigma^\dagger | z^r z'^r \rangle \quad (\text{B39})$$

$$= \sum_z \langle z^{2r} | \sigma^\dagger | z^{2r} \rangle + \sum_{z \neq z'} \langle z^r z'^r | \sigma^\dagger | z^r z'^r \rangle \quad (\text{B40})$$

$$= d_B + d_B(d_B - 1) \delta_{\sigma^\dagger, \sigma_1 \sigma_2}, \quad \sigma_1, \sigma_2 \in S_r. \quad (\text{B41})$$

Then the first part in Eq. (B37) is

$$\text{Wg}(e, 2r)d_A^{2r}(\tau|D_r^{\otimes 2})_B|\tau\rangle_A|D_r^{\otimes 2})_B = \text{Wg}(e, 2r)d_A^{2r}d_B|\tau\rangle_A|D_r^{\otimes 2})_B, \quad (\text{B42})$$

which recovers the boundary condition before the backward process. For the second term, the coefficients satisfy  $(\sigma|\tau\rangle_A = \text{tr}(\sigma^\dagger\tau)_A = d^{|\sigma^\dagger\tau|} > 0$  and  $(\sigma|D_r^{\otimes 2}) = \text{tr}(\sigma^\dagger \sum_{z,z'} |z^r\rangle\langle z^r| \otimes |z'^r\rangle\langle z'^r|) \geq 0$ . By discarding any potential existing time-dependent contribution in the second term, we have

$$\mathbb{E}_{\text{Haar}} \left[ \mathcal{F}^{(m,K)}(T) \right] \geq \frac{d_A^2 d_B}{d_A^2 d_B^2 - 1} \mathbb{E}_{\text{Haar}} \left[ \mathcal{F}^{(m,K)}(T-1) \right], \quad (\text{B43})$$

which immediately brings us the lower bound on the pseudo frame potential as

$$\mathbb{E}_{\text{Haar}} \left[ \mathcal{F}^{(m,K)}(T) \right] \geq \left( \frac{d_A^2 d_B}{d_A^2 d_B^2 - 1} \right)^T \mathbb{E}_{\text{Haar}} \left[ \mathcal{F}^{(m,K)}(0) \right] = \left( \frac{d_A^2 d_B}{d_A^2 d_B^2 - 1} \right)^T. \quad (\text{B44})$$

Here we have used the initial condition  $\mathbb{E}_{\text{Haar}} \left[ \mathcal{F}^{(m,K)}(0) \right] = 1$ . Lemma 2 is thus proved by taking the limit of  $m \rightarrow 1 - K$ .

We next takes an approximation to precisely handle the second term. We consider a subset of permutations  $\sigma \in \mathcal{S}$  such that

$$|D_r^{\otimes 2})(0^{2r}|\mathbb{E}[(U \otimes U^\dagger)^{\otimes 2r}]|\sigma\rangle_A|D_r^{\otimes 2})_B \propto |\sigma\rangle_A|D_r^{\otimes 2})_B \quad (\text{B45})$$

in the leading order. These permutations will remain invariant through the following unitary twirlings which contribute to the time-invariant term in the recurrent equation, modeled as a constant  $q$ . Therefore, we have

$$\mathbb{E}_{\text{Haar}} \left[ \mathcal{F}^{(m,K)}(T) \right] \geq \text{Wg}(e, 2) \left( d_A^2 d_B \mathbb{E}_{\text{Haar}} \left[ \mathcal{F}^{(m,K)}(T-1) \right] + q \right) \quad (\text{B46})$$

$$= \frac{1}{d_A^2 d_B^2 - 1} \left( d_A^2 d_B \mathbb{E}_{\text{Haar}} \left[ \mathcal{F}^{(m,K)}(T-1) \right] + q \right) \quad (\text{B47})$$

$$= \frac{d_A^2 d_B}{d_A^2 d_B^2 - 1} \mathbb{E}_{\text{Haar}} \left[ \mathcal{F}^{(m,K)}(T-1) \right] + \frac{q}{d_A^2 d_B^2 - 1}, \quad (\text{B48})$$

where  $q$  is defined as

$$q = \sum_{\sigma \in \mathcal{S}, \sigma \neq \tau} (\sigma|\tau\rangle_A (\sigma|D_r^{\otimes 2})_B, \quad (\text{B49})$$

which is a positive constant. The pseudo frame potential can thus be solved as

$$\mathbb{E}_{\text{Haar}} \left[ \mathcal{F}^{(m,K)}(t) \right] \geq (1 - q) \left( \frac{d_A^2 d_B}{d_A^2 d_B^2 - 1} \right)^t + q. \quad (\text{B50})$$

where we redefine  $q \rightarrow q/(d_A^2(d_B - 1)d_B - 1)$  for simplicity. In the thermodynamic limit  $d_A \rightarrow \infty$ , it can be further reduced to

$$\mathbb{E}_{\text{Haar}} \left[ \mathcal{F}^{(m,K)}(t) \right] \geq (1 - q) \left( \frac{1}{d_B} \right)^t + q, \quad (\text{B51})$$

where  $q = (1 + (2^K - 1)/d_B)\mathcal{F}_{\text{Haar}}^{(K)}$  is found empirically.

### Appendix C: Additional details on quantum circuit size

In this section, we discuss the scaling of quantum circuit size with different choices of  $N_B$  in holographic deep thermalization in detail. For convenience, we reprint the definition of quantum circuit size here

$$\text{Q-size} \equiv \text{depth per step} \times T \times (N_A + N_B) \quad (\text{C1})$$

$$\propto T \times (N_A + N_B)^2, \quad (\text{C2})$$

where the second line from the unitary design [10, 26].

To generate an  $\epsilon$ -approximate  $K$ -design state ensemble in holographic deep thermalization, we need  $N_B \gtrsim K + \log_2(1/\epsilon)$ . Following Eq. (10), we notice that the minimum quantum circuit size is achieved at  $N_B = N_A$  as

$$\text{Q-size}|_{N_B=N_A} \gtrsim 4N_A \left[ KN_A - \log_2(K!) + \log_2 \left( \frac{1}{\epsilon - (2^K - 1)2^{-N_A}} \right) \right] \quad (\text{C3})$$

$$\sim 4KN_A^2 + 4N_A \log_2(1/K!\epsilon). \quad (\text{C4})$$

At the minimum necessary bath  $N_B = K + \log_2(1/\epsilon)$ , from the expression of the relative frame potential error,

$$\delta\mathcal{F}^{(K)} = \frac{2^K - 1}{d_B} + d_B^{-T} \frac{1}{\mathcal{F}_{\text{Haar}}^{(K)}} \simeq \frac{2^K - 1}{d_B} + d_B^{-T} \frac{d_A^K}{K!} = \epsilon, \quad (\text{C5})$$

we can solve the necessary time steps

$$T|_{N_B=K+\log_2(1/\epsilon)} = K \frac{N_A}{N_B} - \frac{1}{N_B} \log_2(K!) + 1. \quad (\text{C6})$$

Then the quantum circuit size becomes

$$\text{Q-size}|_{N_B=K+\log_2(1/\epsilon)} \propto T(N_A + N_B)^2 \quad (\text{C7})$$

$$= (KN_A - \log_2(K!) + K + \log_2(1/\epsilon)) \left( \frac{N_A}{K + \log_2(1/\epsilon)} + 1 \right) (N_A + K + \log_2(1/\epsilon)). \quad (\text{C8})$$

On the other hand, for  $T = 1$  corresponding to the conventional deep thermalization, in order to guarantee small error

$$\delta\mathcal{F}^{(K)} = \frac{1}{d_B} \left( 1 + \frac{1}{\mathcal{F}_{\text{Haar}}^{(K)}} \right) \simeq \frac{1}{d_B} \left( 1 + \frac{d_A^K}{K!} \right) \leq \epsilon, \quad (\text{C9})$$

we require

$$N_B \gtrsim \log_2 \left( 1 + \frac{d_A^K}{K!} \right) + \log_2(1/\epsilon) \simeq KN_A - \log_2(K!) + \log_2(1/\epsilon), \quad (\text{C10})$$

where the first line we utilize the result from Ref. [24], which is slightly more precise than our result. The quantum circuit size for conventional deep thermalization is

$$\text{Q-size}|_{N_B=KN_A-\log_2(K!)+\log_2(1/\epsilon)} = [(K+1)N_A - \log_2(K!) + \log_2(1/\epsilon)]^2, \quad (\text{C11})$$

which is always a quadratic scaling in  $N_A$ .

To compare the quantum circuit size requirement in Eq. (C8) and Eq. (C11), we can analytically solve the critical  $N_A^*(K, \epsilon)$  such that their quantum circuit size is equal. To reveal the scaling of  $N_A^*(K, \epsilon)$  explicitly, we have

$$(KN_A - \log_2(K!) + K + \log_2(1/\epsilon)) \frac{(N_A + K + \log_2(1/\epsilon))^2}{K + \log_2(1/\epsilon)} = ((K+1)N_A - \log_2(K!) + \log_2(1/\epsilon))^2 \quad (\text{C12})$$

$$(KN_A - K + K + \log_2(1/\epsilon)) \frac{(N_A + K + \log_2(1/\epsilon))^2}{K + \log_2(1/\epsilon)} = ((K+1)N_A + \log_2(1/\epsilon))^2 \quad (\text{C13})$$

$$N_A^*(K, \epsilon) \simeq \frac{1}{2} \left( \sqrt{(K + \log_2(1/\epsilon)) (K^3 + K^2 \log_2(1/\epsilon) + 4 \log_2(1/\epsilon))} + K^2 + K \log_2(1/\epsilon) \right) \quad (\text{C14})$$

where in the second line we take  $\log_2(K!) \rightarrow K$  in the L.H.S and get rid of the one in R.H.S. for convenience. Eq. (C14) indicates that the critical system size  $N_A^*(K, \epsilon)$  undergoes a continuous transition from approximation-error-dependent scaling  $\sim K \log_2(1/\epsilon)$  to universal scaling  $K^2$  with increasing order  $K$  shown in Fig. 9, and we can roughly estimate the transition point to be  $K \sim \log_2(1/\epsilon)$ . The threshold can be summarized as

$$N_A^*(K, \epsilon) = \begin{cases} K \log_2(1/\epsilon), & \text{if } K \ll \log_2(1/\epsilon); \\ K^2, & \text{if } K \gg \log_2(1/\epsilon). \end{cases} \quad (\text{C15})$$

When  $N_A \geq N_A^*(K, \epsilon)$ , the minimum bath case requires higher quantum circuit size, otherwise conventional deep thermalization requires higher quantum circuit size.

In the following, we analyze the scaling of quantum circuit size with  $K \leq \log_2(1/\epsilon)$ .

For  $K < \log_2(1/\epsilon)$ , the quantum circuit size of minimum bath scales as

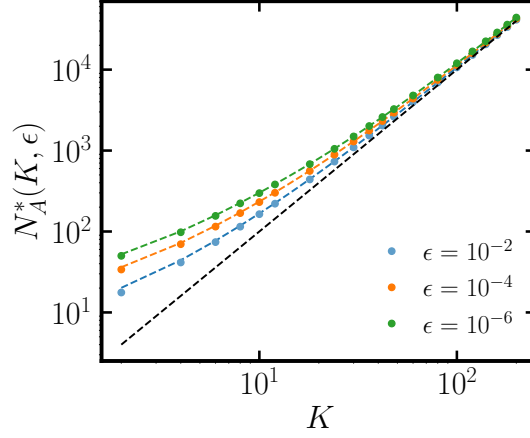


Figure 9. The critical system size  $N_A^*(K, \epsilon)$  for quantum circuit size with minimum bath equals conventional deep thermalization. Colored dots represent  $N_A^*(K, \epsilon)$  with different  $\epsilon$ . Colored dashed lines represent the solution from Eq. (C14) with corresponding  $\epsilon$ , and black dashed line indicate the scaling of  $\sim K^2$ .

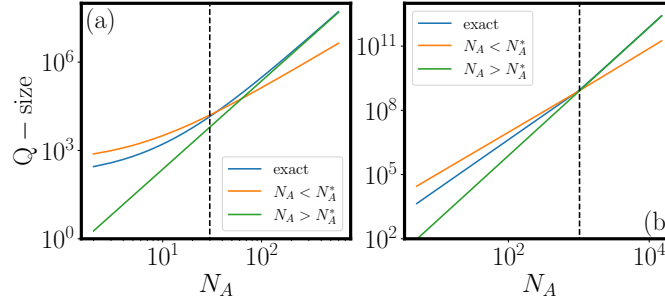


Figure 10. The scaling of quantum circuit size with minimum bath for (a)  $K < \log_2(1/\epsilon)$  and (b)  $K > \log_2(1/\epsilon)$ . Parameters:  $\epsilon = 10^{-3}$ ; (a)  $K = 3$  (b)  $K = 32$ . Blue lines show exact result in Eq. (C8). Orange lines represent scaling analyses as (a)  $(K+1)(KN_A + \log_2(1/\epsilon))(N_A + \log_2(1/\epsilon))$  and (b)  $K^3(N_A + 1 - \log_2(K))(N_A + K)/(K + \log_2(1/\epsilon))$ . The green lines represent  $KN_A^3/(K + \log_2(1/\epsilon))$ . Black vertical dashed lines indicate (a)  $N_A^* \sim K \log_2(1/\epsilon)$  and (b)  $N_A^* \sim K^2$ .

1.  $N_A < N_A^* = K \log_2(1/\epsilon)$ . Q-size  $\simeq (K+1)(KN_A + \log_2(1/\epsilon))(N_A + \log_2(1/\epsilon))$ .
2.  $N_A > N_A^* = K \log_2(1/\epsilon)$ . Q-size  $\simeq \frac{KN_A^3}{K + \log_2(1/\epsilon)}$ .

On the other hand for  $K > \log_2(1/\epsilon)$ , the quantum circuit size of minimum bath scales as

1.  $N_A < N_A^* = K^2$ . Q-size  $\simeq (KN_A - \log_2(K!) + K) \frac{K^2}{K + \log_2(1/\epsilon)} (N_A + K) \simeq \frac{K^3}{K + \log_2(1/\epsilon)} (N_A + 1 - \log_2 K)(N_A + K)$ .
2.  $N_A > N_A^* = K^2$ . Q-size  $\simeq \frac{KN_A^3}{K + \log_2(1/\epsilon)}$ .

where we apply  $\log_2(K!) \simeq K \log_2(K)$  in the first line. We demonstrate the above scalings in Fig. 10a and b for the two cases of  $K \lesseqgtr \log_2(1/\epsilon)$  separately.

#### Appendix D: Additional numerical details

In this section, we provide additional details on the numerical simulations. Our simulations on HDT and QML-enhanced HDT are both implemented with TensorCircuit [27].

In Fig. 11, we present the dynamics of *projected ensemble* for other higher order frame potentials, e.g.  $K = 2, 3$ . In Fig. 11ac, provided a fixed bath size  $N_B = 1$ , the convergence rate with different system size  $N_A$  keeps to be the same, and agrees with our prediction of  $\sim 1/d_B^t$  in Lemma. 2 in the main text, which further supports that the inequality

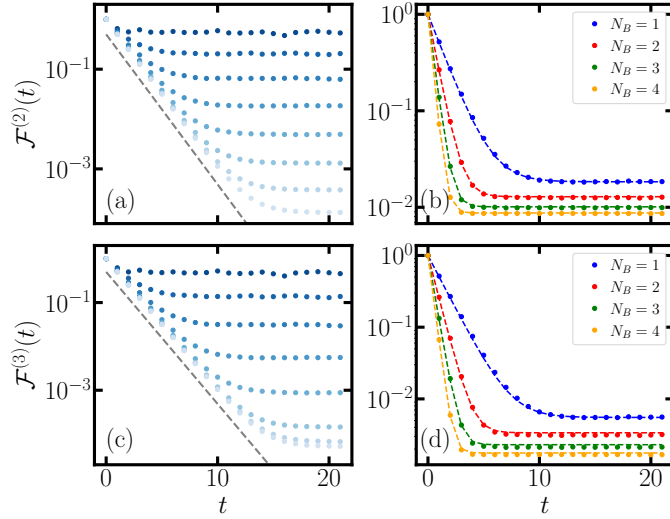


Figure 11. Dynamics of frame potential  $\mathcal{F}^{(K)}$  with  $K = 2$  (top) and  $K = 3$  (bottom). In the left panel (a)(c), the bath size is  $N_B = 1$ . Blue dots from dark to light represent numerical simulation results with system size  $N_A = 1, \dots, 8$ . In the right panel (b)(d), the system size is  $N_A = 4$ . Color dots represent numerical simulation results with bath size  $N_B = 1, \dots, 4$ . Grey dashed lines in (a)(c) show the scaling of convergence  $\sim d_B^{-t}$ . Note that the overlapping dots for small frame potential is due to finite sampling error. Colored dashed lines in (b)(d) represent Eq. (7).

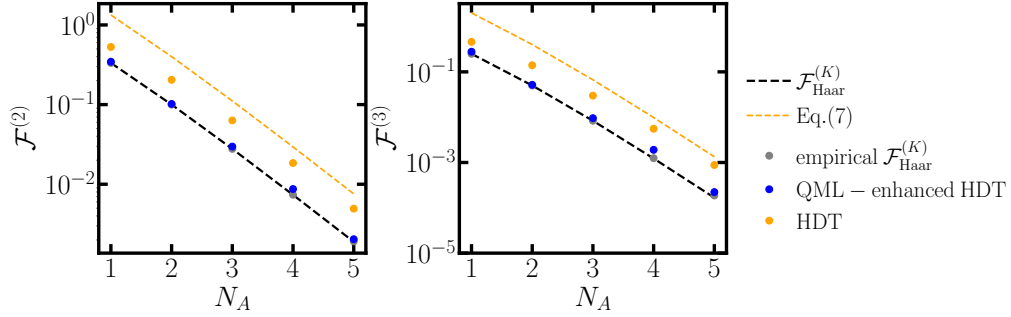


Figure 12. QML-enhanced HDT frame potential  $\mathcal{F}^{(K)}$  with (a)  $K = 2$  and (b)  $K = 3$ . Orange dots represent converged frame potential in HDT with random unitary implementation. Orange dashed line is the theoretical prediction in Eq. (7). Blue dots are frame potential of output state ensemble from QML-enhanced HDT. Black dashed line and gray dots show the exact and empirical of Haar ensemble frame potential.

there is tight. In Fig. 11bc, our predictions in Eq. (7) again agree with the numerical simulation results, indicating that Eq. (7) characterizes the dynamics of frame potential.

In Fig. 12, we show the frame potential for output state ensemble in QML-enhanced HDT with  $K = 2$  and  $K = 3$ , and we still find the constant advantage from QML enhancement (blue dots) compared to the random unitary implementation (orange dots). A comprehensive study on the advantage provided by QML is an interesting open question, especially its dependence on the bath system size and frame potential order  $K$ . The average state based loss function is experimentally friendly for large number of iterations though it may lose the full control over the ensemble property compared to other state-wise measures, especially when the number of steps is limited.

### Appendix E: Additional details on noisy simulation

In this section, we provide additional details on the noisy simulation based on IBM Quantum devices. The noisy simulation is implemented with Qiskit [23] and PennyLane [28].

To understand the gap of frame potential between the ideal theory prediction and noisy simulations, we can consider a depolarizing noise model  $\rho \rightarrow (1 - \gamma)\rho + \gamma\mathbf{I}/d_A$  where  $\rho$  is the ideal average state and  $\mathbf{I}/d_A$  is the maximally mixed

state and  $\gamma$  is the noise probability. The purity then becomes

$$\text{tr}(\rho^2) \rightarrow \text{tr}\left[\left((1-\gamma)\rho + \gamma\mathbf{I}/d_A\right)^2\right] \quad (\text{E1})$$

$$= (1-\gamma)^2 \text{tr}(\rho^2) + 2\gamma(1-\gamma)\frac{1}{d_A} + \gamma^2\frac{1}{d_A} \quad (\text{E2})$$

$$= (1-\gamma)^2 \text{tr}(\rho^2) + \frac{(2-\gamma)\gamma}{d_A}, \quad (\text{E3})$$

where  $\text{tr}(\rho^2)$  in the first term is the ideal purity and second term is the contribution from maximally mixed state mixture. As  $\gamma \in [0, 1]$ , the purity is monotonically decreasing with increasing to noise probability, which agrees with a naive physical understanding on depolarizing noise channel. In the main text, we take  $\gamma \simeq 0.07$  in the noise-corrected theory.

---